Optical Measurements of TES Bolometers for SAFARI

Michael D. Audley, Axel Detrain, Lorenza Ferrari, Jian-Rong Gao, Darren Hayton, Gert de Lange, Philip D. Mauskopf, Dmitry Morozov, Manisha Ranjan Neil A. Trappe, and Willem Jan Vreeling

Abstract— **We have measured the optical response of detectors for SAFARI, the far-infrared imaging spectrometer for the SPICA satellite. SAFARI's three bolometer arrays, coupled with a Fourier transform spectrometer, will provide images of a 2'×2' field of view with spectral information in three bands covering the wavelength range 34—210 μm. Each bolometer consists of a transition edge sensor (TES) with a transition temperature close to 100 mK and a resistive absorber on a thermally-isolated silicon nitride membrane. Each detector sits behind a concentrating horn and in front of a hemispherical backshort. SAFARI requires extremely sensitive detectors (*NEP*~2×10^{-19} W/√Hz) to take advantage of SPICA's cooled optics. To meet the challenge of testing such sensitive detectors we have constructed an ultra-low background test facility with a cryogen-free high-capacity dilution refrigerator, paying careful attention to stray-light exclusion. The SAFARI Detector System Test Facility provides a high degree of electrical, magnetic, and mechanical isolation for the detectors, allowing us to use a pulse-tube cooler to pre-cool the dilution refrigerator. We have verified the test facility's performance in terms of background power loading and carried out cross-calibrations with other test systems. The SAFARI Detector Test Facility is now being used for routine dark and optical measurements of ultra-sensitive TES bolometers. We report on optical measurements of prototype SAFARI detectors.**

***Index Terms*—Bolometers, infrared detectors, superconducting devices, immunity testing, calibration**

I. Introduction

THE Japanese Space Agency's satellite observatory SPICA will use a large (3.5-m diameter) primary mirror cooled to <6 K to enable high angular-resolution, sky-background limited observations of the cold dusty Universe in the mid- and far-infrared [1]. The mission promises to revolutionize our knowledge of the origin and evolution of galaxies, stars and planetary systems. The SAFARI [2] instrument is a far-infrared imaging Fourier transform spectrometer (FTS) for the SPICA satellite. SAFARI has three detector arrays with a total of ~6000 pixels for a Nyquist-sampled field of view of 2'×2' covering the wavelength ranges 34—60 (short wave), 60—110 (medium wave), and 110—210 μm (long wave). The detectors are Transition Edge Sensor (TES) bolometers [3]. The Ti/Au bilayer TES and a Ta absorber are suspended on thin (<1-μm) silicon nitride membrane (see Fig. 1). SAFARI will provide wide-field spectroscopic maps in the far infrared, giving us the ability to study the dynamics and chemistry of a wide range of objects. To take advantage of SPICA's low-background cold mirror, SAFARI's short-wave detectors require a dark noise equivalent power (*NEP*) less than 6.5×10^{-19} W/√Hz, with a goal *NEP* of ~2×10^{-19} W/√Hz. This is over two orders of magnitude more sensitive than TES bolometers previously developed for ground-based applications [4] and the SAFARI detectors have correspondingly low saturation powers (~5 fW).

Testing such sensitive detectors is challenging and requires careful attention to magnetic and RF shielding, stray-light exclusion, and vibration isolation. We have built a test facility which will be used to qualify and characterize the SAFARI focal plane units and readout before they are integrated into the instrument. In addition to the strict requirements on background and interference, we require that this facility be flexible and re-configurable so that we can use it for dark and optical tests of single pixels through to the full focal-plane arrays. Through a systematic program of incremental modifications we have improved the performance of the SAFARI Detector Test Facility to the point where it is capable of testing SAFARI's ultra-sensitive bolometer arrays. The test facility is now being used for routine measurements of prototype SAFARI detectors. We have measured the optical response of two prototype detectors designed for SAFARI's short-wave band (33—60 μm) array. These are of the type shown in Fig. 1, and have moderate sensitivity (NEP = 1—2 aW/√Hz). While these detectors have been far surpassed in sensitivity by the latest detectors for SAFARI, they absorb radiation in the same way [5], and are thus representative for optical characterization.

Manuscript received August 15, 2012.

M. D. Audley L. Ferrari, A. Detrain, D. Hayton, G. de Lange, M. Ranjan, and W. J. Vreeling are with SRON Netherlands Institute for Space Research, 9747 AD Groningen, The Netherlands (phone: +31(0)50-363-9361; fax: +31-(0)50-363-4033; e-mail: audley@physics.org).

J.-R. Gao is with SRON Netherlands Institute for Space Research, 3584 CA Utrecht, The Netherlands.

J.-R. Gao is with the Kavli Instiurte of Nanoscience, Faculty of Applied Sciences, Delft University of Technology, 2628 CJ Delft, The Netherlands.

N. A. Trappe is with the Experimental Physics Department, National University of Ireland, Maynooth, Co. Kildare, Ireland.

D. Morozov and P. D. Mauskopf were with the Department of Physics and Astronomy, University of Cardiff, Cardiff CF24 3YB, United Kingdom.

P. D. Mauskopf is now with the Physics Department, Arizona State University, Tempe, AZ 85287 USA.

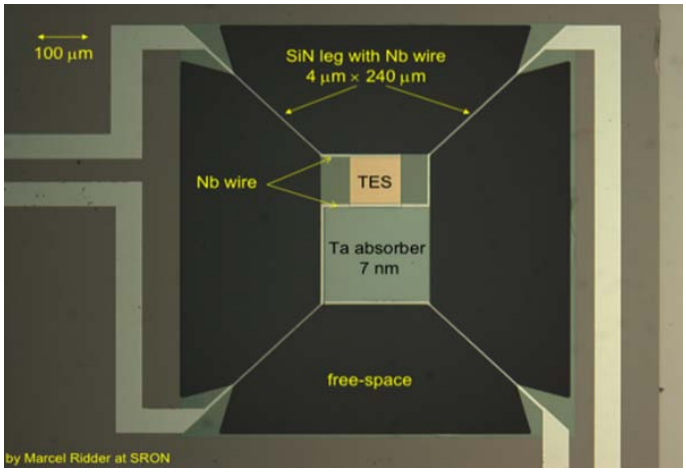

Fig. 1. Photograph of a TES detector similar to the ones measured here.

II. Description of the Test Facility

The SAFARI Detector Test Facility is based on a Leiden Cryogenics dilution refrigerator with a cooling power of ~200 μW at 100 mK [6]. We have found that we can reach a base temperature on the mixing chamber below 8 mK and have operated detectors in the dark with bath temperatures, T_{bath}, as low as 15 mK. This bath temperature is well below the value required for testing the SAFARI detectors and gives us plenty of headroom for experiments that place additional heat loads on the system, e.g. black-body illuminator. The refrigerator uses no expendable cryogens and is precooled by a Cryomech PT-415 pulse-tube cooler which is attached to the 50-K and 3-K stages of the cryostat. To mitigate the effects of vibrations, the pulse-tube cooler has two expansion tanks and its rotary valve motor is separated from the cryostat. The expansion tanks and valve motor are mounted on the cryostat's support tripod. One advantage of using a mechanical cooler is that it is closer to the flight configuration which also uses mechanical cooling than a wet cryostat would be. The main disadvantage is that we need to protect the detectors under test from mechanical and electrical interference from the cooler. For detector readout and thermometry there are eight woven looms of 12 twisted pairs. Two have Cu conductors for low electrical resistance (and hence low Johnson noise) and are used for the SQUID bias. The rest have CuNi conductors to minimize thermal conductance. The looms are enclosed in stainless steel tubes and heatsunk at various points. RF shielding is provided by two nested Faraday cages. The outer one is formed by the Dewar main shell and contains the room-temperature readout electronics as well as a multiplexer box, which allows us to connect the readout to different SQUIDs. The inner Faraday cage is the 3-K shield. Wires entering the 3-K shield are low-pass filtered at several hundred MHz. The system has been designed for flexibility: a reconfigurable patch board on the 8-mK stage redistributes the signals from the looms between the two experiment boxes currently installed. One of these experiment boxes is being used for dark testing and system optimization. The other is used for optical detector testing and provides the results presented here.

Each experiment box comprises a tin-plated copper can, with light-tight feedthrough for wiring and an absorbing labyrinth where it attaches to its base, all surrounded by a Cryoperm can (see Fig. 2). We have verified that this provides good magnetic shielding and is light-tight. We had originally intended to replace the tin-plated copper can with a niobium can, but we found that the copper can provided adequate magnetic shielding with the advantage over niobium of a high thermal conductivity.

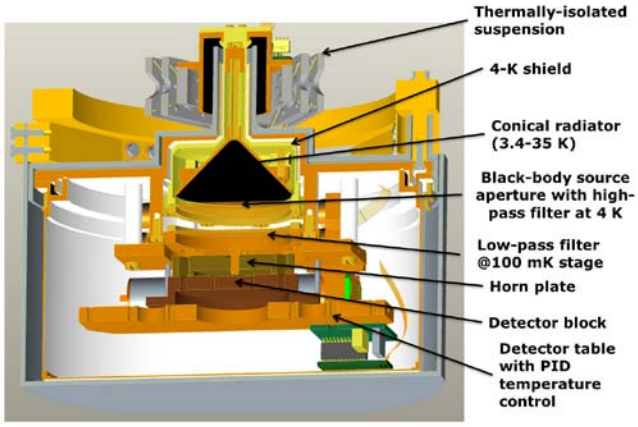

Fig. 2. Cutaway view of detector box showing the black-body illuminator and detector table inside the nested shields. The diameter of the outer, Cryoperm shield is 15 cm.

III. Optimization of the Test Facility

Our challenge was to build an ultra-low background test facility that still had the flexibility to accommodate the various experiments that will be needed until the SAFARI focal plane arrays have been fully characterized. Starting with a well-engineered system, we carried out a comprehensive program of optimization, making improvements to the system in small steps until we arrived at the point where were confident that the system was suitable for testing ultra-sensitive TES bolometers.

The optimization program comprised many small improvements that came under four general areas. First, we took some steps to mitigate the effect of vibrations and electrical interference from the pulse-tube cooler. We replaced the hose between the rotary valve and the cold head with a longer one that could accommodate the motion of the valve. We also replaced the square-wave driver for the rotary-valve motor with a linear drive. Second, we paid careful attention to eliminating ground loops. We isolated the gas-handling system electrically from the cryostat and instrument rack. Third, we ensured that the signal wiring inside the cryostat was immobilized as much as possible. Because this system is a test bed and needs to be flexible, it was not always possible to use rigid conductors everywhere. Any wiring associated with the input circuits of the SQUIDs was made from the stiffest wire available and shielded with superconducting Al tubing. Fourth, we made sure that the Faraday cages were closed as much as possible. We found that opening one of the boxes surrounding the room-temperature readout electronics increased the loading on the detectors by several fW. There is still room for improvement here.

To confirm the low-noise performance of the system, we mounted an ultra-sensitive TES fabricated at SRON in the test facility. This particular detector had previously been characterized in a different low-background test facility [7], [8]. We found that when the TES is in the superconducting state we see a few lines in the power spectrum, from radio-frequency interference and microphonic pickup, that disappear when the pulse-tube cooler is switched off. These are small compared with the current noise when the TES is biased on the transition and do not interfere with the measurement of the detector NEP. We were thus able to conclude that the SAFARI Detector Test Facility was ready for characterizing SAFARI's ultra-low NEP detectors.

IV. Optical Test Setup

A. Physical Layout

We measured two detectors of the type shown in Figure 1. Optical measurements of these detectors had previously been carried out in a different test system [7]. These detectors do not have the extreme sensitivity of the latest SAFARI detectors [5], but the way in which radiation couples to the bolometer is the same. The detectors have square Ta absorbers 200 µm on a side. Each detector sits in front of a hemispherical backshort and behind a conical feed horn (see Fig. 3). The horn is 4.5 mm long and the diameters of its entrance and exit apertures are 450 and 46 µm, respectively. The horn is contained in a plate that can be positioned over any of the five detectors on the chip. In front of the horn is a high-pass/low-pass pair of filters. The optical measurement setup is as shown in Fig. 2. The detector block is mounted on a table with a thermometer and heater to allow PID control of the detector-table temperature. The optical source is defined by an aperture in the 3-K shield of the black-body illuminator. This aperture is located 17 mm in front of the horn. The temperature of the illuminator is also controlled by a PID control loop.

We measured the beam pattern of the horn using a 5.3-THz (57-µm) FIR laser and found an angular width of about 9.1° FWHM, in good agreement with the calculated far-field beam pattern at that frequency (see Fig. 5). This gives a beam size at the aperture of the illuminator of about 2 mm (radius) at a wavelength of 50 µm. We carried out the optical measurements of the detectors with two different aperture diameters: 5 mm and 12 mm. The 5-mm aperture has a size comparable to the expected beam size of the horn, which means that the throughput is reduced by the aperture and is sensitive to the alignment between the aperture and horn. With the 12-mm diameter aperture we illuminate the beam of the horn fully, and should be insensitive to small errors in alignment. As expected, we measured a higher throughput than with the 5-mm aperture.

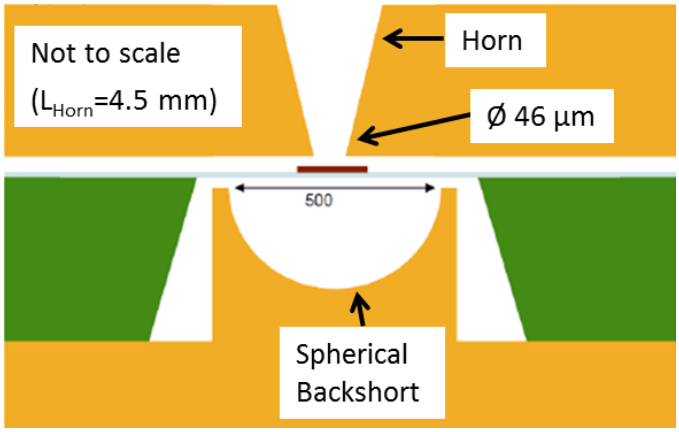

Fig. 3. Cross-section of feedhorn and spherical backshort showing position of detector (not to scale). The diameter of the spherical backshort is 500 µm.

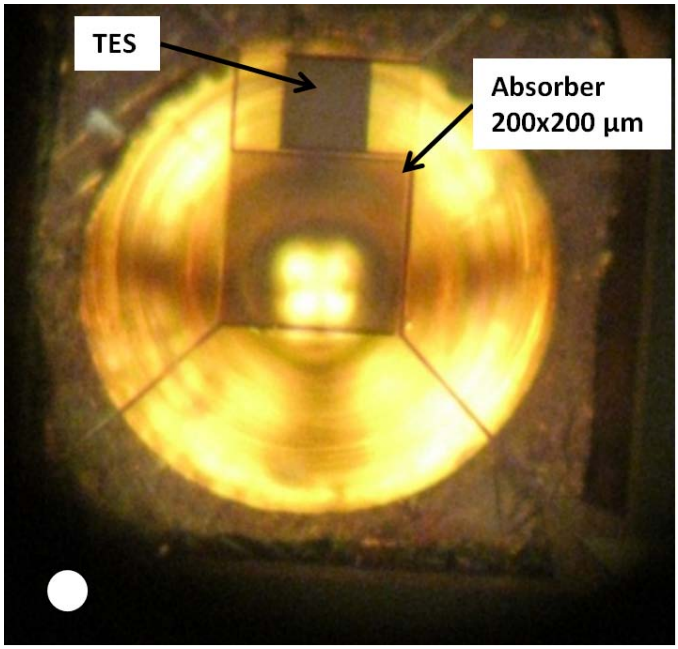

Fig. 4. Photograph of detector sitting above spherical backshort. The white circle in at the lower left represents the footprint of the 46-µm exit aperture of the horn. This has been displaced from its position over the center of the backshort for clarity.

B. System Throughput

In order to measure the absorption efficiency of the combination of detector, backshort, and horn, it is necessary to estimate the incident power from the illuminator accurately. The horn's 46-µm diameter exit aperture should block wavelengths longer than about 90 µm. This small exit aperture was chosen for these tests so that it would act as a mode filter. Given the band-pass of our filter stack (33—50 µm), and the low temperature of the black-body illuminator (< 32 K to saturate the detectors), we make the assumption of only a single mode propagating through the horn. In the case of a large source aperture, where the beam of the horn is fully illuminated, we expect the throughput of the system to be $A\Omega=\lambda^2$. The power incident on the detector is then (assuming a source emissivity of 1)

$$P_{\mathrm{inc}}(T) = \int \frac{2hc^2}{\lambda^5} \frac{1}{e^{\frac{hc}{\lambda kT}} - 1} \tau(\lambda) \lambda^2 d\lambda \quad (1)$$

where τ(λ) is the measured transmission of the filter stack. The efficiency of the horn-cavity-detector combination is then

$$\eta = \frac{P_{\mathrm{det}}(T)}{P_{\mathrm{inc}}(T)} \quad (2)$$

where $P_{\mathrm{det}}(T)$ is the detected optical power at illuminator temperature T. If the source aperture is not large compared to the size of the horn's beam the throughput will be reduced by a factor of $1-\exp(-2(r_{\mathrm{ap}}/w(\lambda))^2)$ where r_{ap} is the radius of the aperture and $w(\lambda)$ is the beam radius [9]. The throughput will be further reduced if there is also an offset between the centers of the horn and the aperture.

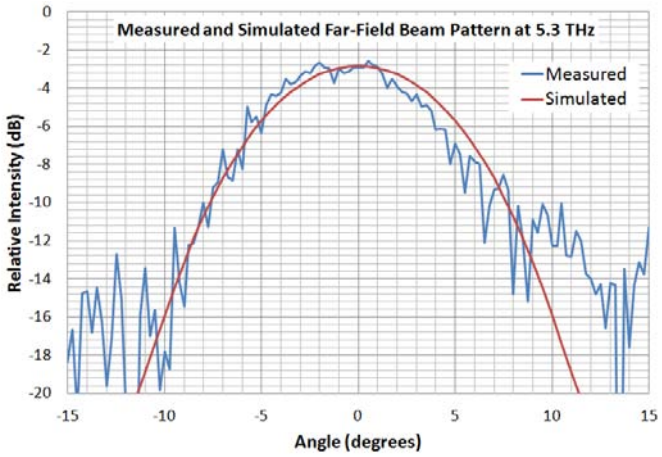

Fig. 5. Measured and simulated beam pattern of horn. The beam has a FWHM of 9.1°.

V. Measurements

A. Readout and calibration

Each TES detector was voltage-biased using a shunt resistor of 1—2 mΩ and the TES current was read out using a Superconducting Quantum Interference Device (SQUID). We used single-stage SQUIDs from PTB [10] with Magnicon readout electronics [11]. The SQUIDs and shunt resistors were mounted on the detector table at the same temperature-stage as the detectors. The shunt resistors were formed from short gold wire bonds. The resistance of the shunt resistor was verified from its Johnson noise power spectrum.

B. IV Curves

We measured current-voltage characteristic curves (IV curves) of the detectors at different bath temperatures and used the known component values of the bias circuit to produce calibrated IV curves which show the current through the TES against the voltage across it (Fig. 6). We then calculated the Joule power, P_{Joule}, at each TES voltage, V_{TES}, to convert the IV curves into power curves: $P_{\mathrm{Joule}}=V_{\mathrm{TES}}I_{\mathrm{TES}}$, where I_{TES} is the TES current. Each power curve comprises a parabolic region corresponding to the normal state, a flatter region commonly called the power plateau [12] where the TES is on the transition, and a point at the origin corresponding to the superconducting state. Examples are shown in Fig. 7 where the Joule power is plotted against the absolute value of the TES voltage. The data corresponding to positive and negative voltages coincide almost exactly, verifying that the calibration is good.

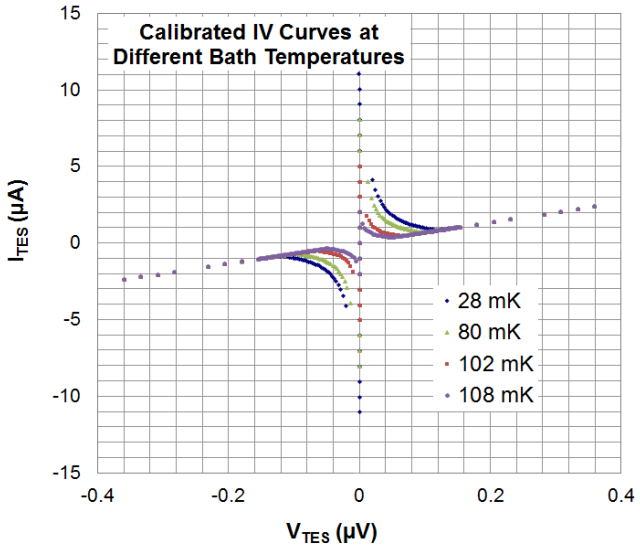

Fig. 6. Calibrated IV curves at different detector-table temperatures for detector 17E.

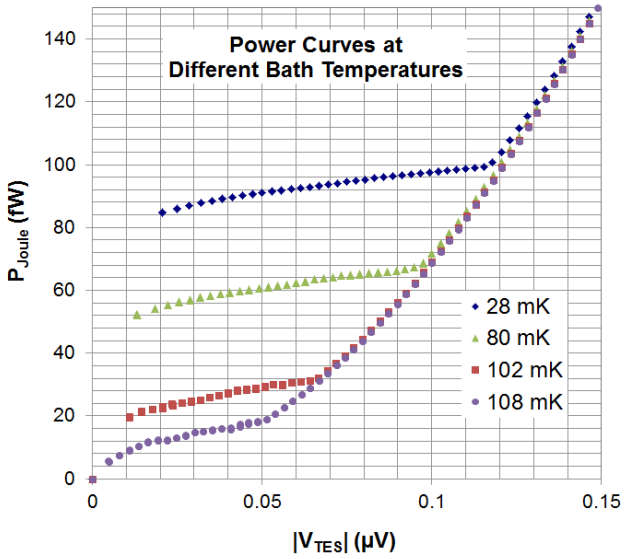

Fig. 7. Power Curves at different detector-table temperatures for detector 17E, calculated from the IV curves in Fig. 6. The Joule power dissipated in the TES is plotted against the absoulute value of the voltage across the TES. Note how the data points corresponding to bias voltages of opposite signs are almost coincident.

We used the power plateaus to estimate the Joule power at each bath temperature, T_{bath}, and fitted the results to a function of the form $P = K(T_c^n - T_{\mathrm{bath}}^n)$ to obtain the transition temperature T_c and thermal conductance $G=nKT_c^{n-1}$ of each detector. This is the model plotted in Fig. 8. The best-fit thermal parameters are shown in Table I, which also shows the measured dark NEP.

TABLE I

MEASURED THERMAL PROPERTIES FOR THE TWO DETECTORS

Parameter	Detector:	17D	17E
Power-flow Exponent: n		3.07	3.15
Power-flow Factor: K (pW/K^n)		89	92
Transition Temperature: T_c (mK)		115	114
Thermal Conductance: G (pW/K)		3.1	2.7
NEP_{dark} (aW/√Hz)		1.7	1.7

For optical measurements we regulated the detector-table temperature at a fixed value (usually 70 mK) and recorded IV curves at different illuminator temperatures. The power dissipated in the illuminator loads the refrigerator and raises its base temperature. The detector-table temperature of 70 mK was chosen so that it could be maintained even when the illuminator was hot enough to saturate the detectors with radiation. From the power plateaus we could calculate the Joule power dissipated in the detector at each illuminator temperature. As can be seen in Fig. 8, optical loading has the effect of depressing the power plateaus. The absorbed optical power at each temperature is then the difference between the power plateau when the illuminator is off and the power plateau at that temperature. In these estimations we consider the illuminator to be off when its temperature is below 3.5 K.

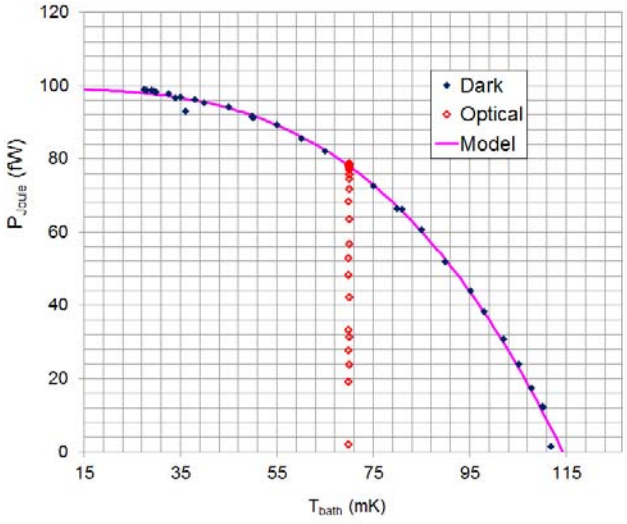

Fig. 8. Measured power plateaus at different bath temperatures in the dark and at fixed bath temperature (70 mK) with optical illumination.

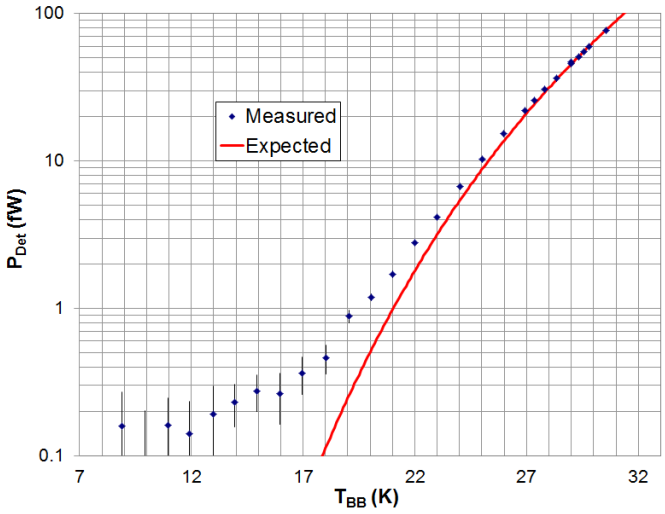

Fig. 9. Absorbed optical power, P_{Det}, calculated from the data in Fig. 8, compared with expected power at different illuminator temperatures, T_{BB}.

We find good agreement between measured and expected power at high illuminator temperatures, but at low illuminator temperatures there is an apparent excess in the detected power (see Fig. 9). This is almost certainly due to a long-wavelength light leak through the filters on the 8-mK shield. This is discussed in Section VII.B.

C. Fixed TES Bias

IV curves give us well-calibrated, precise measurements of the absorbed power, but they can be time-consuming. We need the illuminator temperature to be steady for the duration of the IV-curve acquisition. In principle, this should present no problem, but at high illuminator temperatures the illuminator time constant becomes very long, which means that we must wait a long time for the temperature to settle down. An alternative approach is to allow the illuminator temperature to vary slowly and record data quickly at a few discrete TES bias values. This gives much finer resolution on illuminator temperature and a more precise measurement of the dependence of absorbed power on illuminator temperature. In particular, this allows us to investigate in detail the temperature-dependence of the excess power detected at low illuminator temperatures. The raw data from such a measurement are shown in Fig. 10. Each point on this plot corresponds to a single point used to build up an IV curve, which gives us a considerable time saving over taking a full IV curve at each illuminator temperature. As expected, the dark pixel has a much smaller response to illumination. The illuminated pixel can be seen to saturate at different temperatures, depending on how high on the transition it is biased. We can convert these data into absorbed power in the same way as for IV curves. The absorbed power for a single TES bias voltage is shown in Fig. 11. Although the dark pixel sees less power than the optical pixel, both pixels have an almost identical linear dependence of the absorbed power on illuminator temperature for low illuminator temperatures (the ratio is shown in Fig. 12). We discuss possible causes for this in Section VII.B.

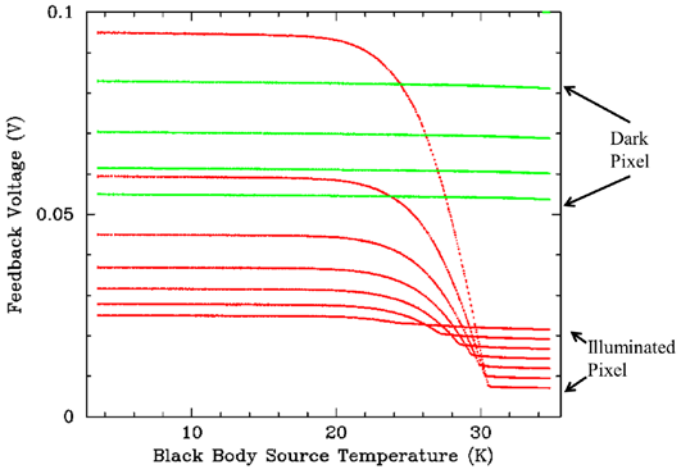

Fig. 10. Response of flux-locked-loop feedback voltage to optical illumination for dark and illuminated pixels at different bias. Some of the dark-pixel traces have been omitted for clarity.

Fig. 13 shows the response of the optical pixel with the power detected in the dark pixel subtracted. The noise floor estimated from the bandwidth of the measurement and the NEP of the detector is also shown. With the dark pixel subtracted, power becomes undetectable around the noise-floor level, showing that the excess at low illuminator temperatures has been effectively subtracted. However, this correction subtracts too much power at high illuminator temperatures where the 2.6% optical crosstalk is significant. Aside from this over-subtraction, the estimated detected optical powers in Fig. 13 are lower than predicted for high illuminator temperatures. This is due to the fact that when the TES is biased at a fixed voltage, the resistance of the TES (and hence the actual bias point on the transition) will depend on the external power loading. Since the power plateaus in Fig. 7 are not flat the Joule power dissipated in the TES depends on the TES resistance. This effect is not seen when estimating the absorbed power from IV curves if care is taken to ensure that the power plateau is always measured at the same point on the transition (i.e. the same TES resistance).

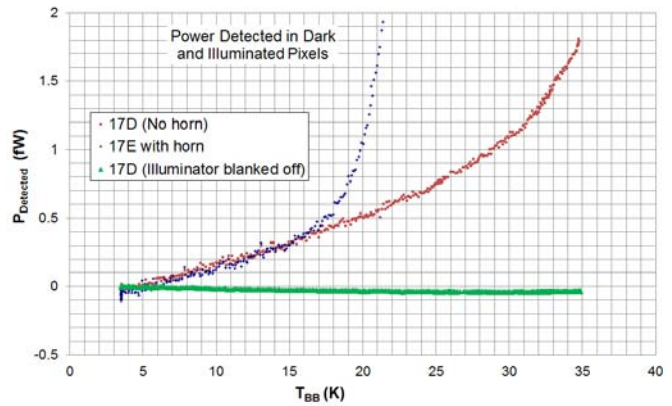

Fig. 11. Absorbed power vs illuminator temperature in the dark pixel (squares), illuminated pixel (diamonds), and with the illuminator closed off with a blanking plate (triangles).

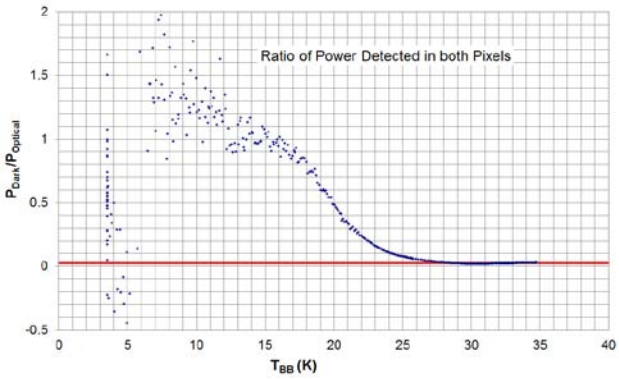

Fig. 12. Ratio of power detected in the dark pixel to that detected in the illuminated pixel. The solid line denotes the ratio above 30 K, which is about 0.026. We interpret this as the level of optical cross-talk between the pixels.

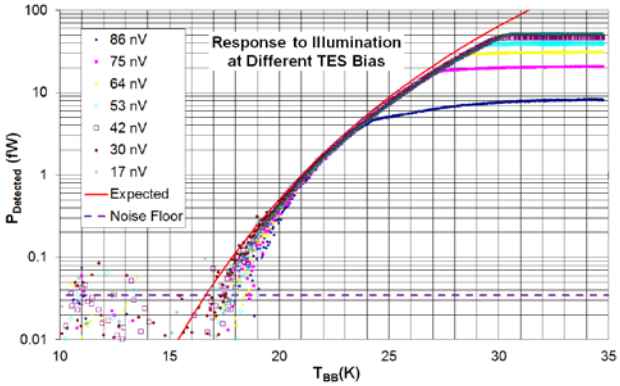

Fig. 13. Response to optical illumination at different fixed TES bias voltages. The detected power, P_{Detected} at each illuminator temperature, T_{BB}, has had the corresponding power detected in the dark pixel subtracted.

D.Photon Noise

We also measured the noise in the detectors at different illuminator temperatures (Fig. 14) and find that the measured photon noise agrees with the value expected from the predicted incident power

$$NEP_{\text{photon}}{}^2(T) = 2\int \frac{hc}{\lambda}\frac{2hc^2}{\lambda^5}\frac{1}{e^{\frac{hc}{\lambda kT}}-1}\tau(\lambda)\lambda^2 d\lambda \qquad (3)$$

and the optical efficiency found from the IV curves and fixed-bias measurements (Fig. 15).

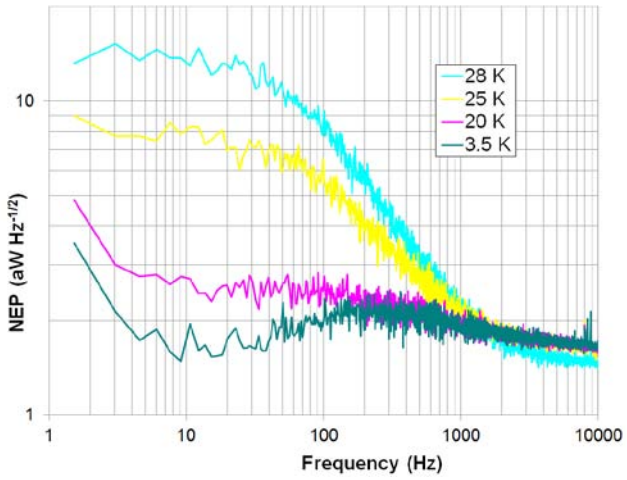

Fig. 14. Photon noise detected at different illuminator temperatures. In this case the detector was biased at $R/R_N \approx 0.34$, where R is the TES resistance at its bias point and R_N is its normal-state resistance.

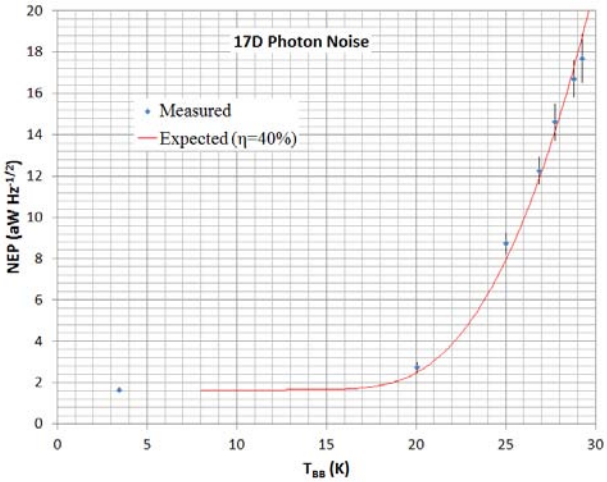

Fig. 15. Measured and expected photon noise.

E. Absorber Resistance

The SAFARI bolometers use a resistive film to couple to incident radiation. Radiation is dissipated in a thin film of Ta and the resulting temperature rise is detected by the TES. For efficient absorption the sheet resistance of this film should be close to the wave impedance of free space (~377 Ω/□). As can be seen in Fig. 1, there are Nb leads connected to the absorber which allow electrical measurements. We attached four wires to the absorber of one of the detectors and measured its resistance as a function of temperature. As shown in Fig. 16, the resistance of the film when in the normal state is 367 Ω, which is close to the required value. Comparing this with a measurement made three years previously, we find that the sheet resistance has increased by 30% in that time. This would suggest that the oxidation of the Ta film is self-limiting and that further passivation measures are not necessary. However, we shall continue to monitor the films over the coming years to confirm this. In Fig. 16 the resistance is plotted against the temperature of the detector table and the apparent transition temperature of the film is about 700 mK, which is lower than the expected value of 900 mK. It is likely that the actual temperature of the nitride island will be higher than the detector-table temperature. Connecting the Ta absorber to the input coil of a SQUID should give us a more accurate estimate of the Ta film's transition temperature, by observing the change in Johnson noise between the resistive and superconducting states.

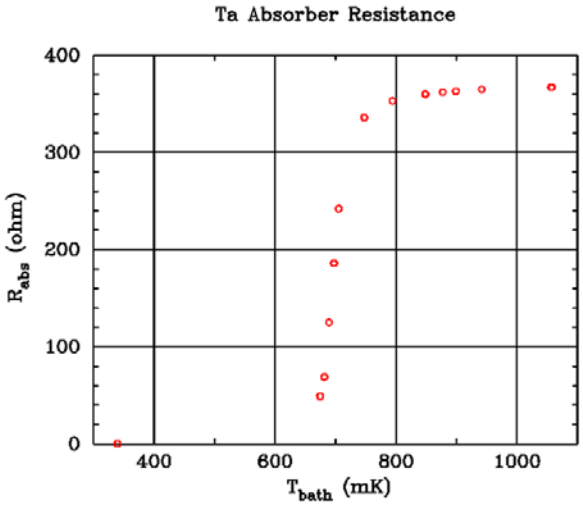

Fig. 16. Measured resistance, R_{abs}, of the Ta absorber on the detector as a function of the temperature of the detector-table, T_{bath}. The normal-state resistance is about 367 Ω.

VI. Future Enhancements of the Test Facility

We have successfully measured the optical response of SAFARI prototype detectors all the way to saturation using the illuminator shown in Fig. 2. However, because of the low temperature of the black-body emitter (3.4—34 K), the passband of the short-wave detectors is illuminated by the Wien tail of the black-body spectrum. This means that only the long-wavelength end of the passband sees significant power. In order to illuminate the passband more uniformly with a black-body source, we need that source to have a much higher temperature. We thus plan to add a hot (200 K) source, with cold attenuation to reduce the power, as shown in Fig. 17. In addition, there will be a light-pipe to room temperature so that we can inject power from an external FTS or a modulated source. A reference detector will allow us to measure the spectral content of the radiation. The reference detector is a TES bolometer, similar to that shown in Fig. 1, suspended in a large absorbing cavity so that its optical absorption coefficient is flat over a broad wavelength range. The light-pipe, reference detector, and hot illuminator are attached to a reflective summing cavity that has a temperature of 4 K. A narrow light pipe leading to a hole in the center of the cold illuminator allows radiation from the summing cavity to illuminate the detectors under test. Both the hot and cold illuminators can be operated during the same cool-down,, allowing cross-calibration. This second-generation optical calibrator has been tested in a 4-K cryostat and will be integrated into the SAFARI Detector Test Facility in preparation for the optical tests of SAFARI prototype detector arrays.

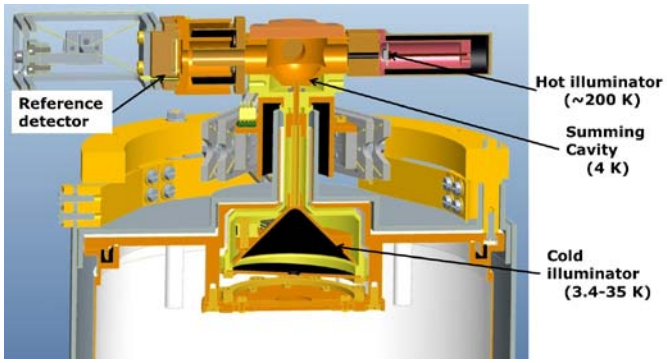

Fig. 17. Second-generation optical illuminator.

VII. Discussion

A. Optical Efficiency

For the two detectors we calculated the optical efficiency from Equation 1, which assumes a single mode propagating through the feedhorn, and Equation 2. We obtained virtually identical efficiencies, η=40%, for both, even though the detectors have slightly different thermal properties. We note that this 40% efficiency is also consistent with the measured photon noise. From electromagnetic simulations we expect the efficiency of the horn/cavity/absorber combination to be 66% at 50 μm. The slightly lower measured value may be due to deviations from the ideal case simulated. In particular, we observe a ~50-μm misalignment between the spherical backshort and the absorber for both detectors. This misalignment might affect the optical efficiency. It is also possible that the gap between the detector and horn is different. Our estimate of the incident power assumes that the radiator is a perfect black body. This estimate is also critically dependent on our knowledge of the high-pass filter that defines the long-wavelength end of the passband.

We also note that the presence of the TES to one side of the absorber may have an effect on the optical efficiency. The sheet resistance of the TES seen by incoming radiation will be very low (~150 mΩ). In particular, it is possible that this could make the setup polarization-dependent. Measurements with a polarizer placed between the feedhorn and the illuminator will detect any polarization dependence.

It should be noted that the configuration tested here is different from that which will be used for the actual SAFARI detector arrays. In particular, instead of single- or few-moded feedhorns, SAFARI will use multi-mode collecting horns to achieve a high filling factor and optical efficiency. The optical efficiencies measured in this work are for a single mode feedhorn.

B. Excess Power at Low Illuminator Temperatures

As Fig. 11 shows, the detected power increases linearly with illuminator temperature in a very similar way for both the optical and dark detectors up to about 15 K. We have investigated this to determine its cause. One possibility we considered was that the current used to heat the illuminator was being detected by the SQUIDs. To check for this we reversed the direction of the current in the illuminator's heaters, but saw no change in the effect. We also ruled out the influence of the detector-table heater as a possible cause by taking data with the temperature free-running and no current through the heater: the effect was unchanged. We also considered whether the effect might be related to thermometry. The difference between the actual bath temperature of the detectors and the detector-table thermometer might depend on the thermal environment which could change as the power in the illuminator is ramped up. Since the thermal conductance of the detectors is about 3 fW/mK, a bath-temperature difference of less than 200 μK could reproduce the apparent 500-aW loading of the dark pixel that we see when the illuminator temperature is 15 K.

One obvious candidate for the cause of this effect is a long-wavelength light leak. We replaced the aperture in the 20-mK shield with a blank copper plate and measured the detected power at different illuminator temperatures. As shown in Fig. 11, the effect then disappeared. This would suggest that the effect is, in fact, due to a long-wavelength light leak. If this is the case, the long-wavelength radiation enters the detector cavities by some route other than through the feedhorn. One possible entry route is the electrical leads to the detectors. These enter the detector block through holes filled with loaded epoxy. The long-wavelength radiation must have a wavelength longer than about 90 μm or it would enter through the feedhorn also and be stronger in the optical pixel. More experiments are planned to investigate and eliminate this effect.

VIII. Conclusion

We have carried out optical measurements of two TES bolometers designed for SAFARI's short-wavelength band (33—60 μm) in combination with a spherical backshort and conical horn. Under the assumption of a single mode propagating through the horn we find an overall optical efficiency of 40% for both detectors, compared with a value of 66% calculated for an ideal model of this combination.

Acknowledgment

This work was made possible by help from Duc van Nguyen, Wim Horinga, and Geert Keizer. We thank Douglas Griffin of the Rutherford Appleton Laboratory for supplying the feedhorn. The detectors and feedhorn used in this work were originally produced for ESA TRP contract no. 22359/09/NL.CP, TES Spectrometer. This work has benefited from results arising from that contract.

References

[1] B. Swinyard., T. Nakagawa., P. Merken, P. Royer, T. Souverijns, B. Vandenbussche, C. Waelkens, et al. "The space infrared telescope for cosmology and astrophysics: SPICA A joint mission between JAXA and ESA." Experimental Astronomy, vol. 23, no. 1, 2008, p.p. 193–219.

[2] B. Jackson, P. de Korte, J. van der Kuur, P. Mauskopf, J. Beyer, M. Bruijn, A. Cros, et al "The SPICA-SAFARI Detector System: TES Detector Arrays With Frequency-Division Multiplexed SQUID Readout," IEEE Transactions on Terahertz Science and Technology, vol. 2, no. 99, 2011, p.p. 1–10.

[3] K. D. Irwin and G. C. Hilton,. “Transition-edge sensors”, in *Cryogenic Particle Detection*, C. Enss, Ed., Springer, 2005, p.p. 81-97.

[4] M. D. Audley, D. M. Glowacka, D. J. Goldie, V. N. Tsaneva, S. Withington, L. Piccirillo, G. Pisano, et al. “Performance of a Microstrip-coupled TES Imaging Module for CMB Polarimetry,” in *Proc. Twenty-First International Symposium on Space Terahertz Technology*, 2010, p.p. 76–84.

[5] P. Khosropanah, R. Hijmering, M. Ridder, J.-R. Gao, D. Morozov, P. D. Mauskopf, N. Trappe, et al. “TES Arrays for the Short Wavelength Band of the SAFARI Instrument on SPICA,” in Proc. SPIE, 2012, submitted for publication.

[6] Leiden Cryogenics BV, Galgewater 21, 2311 VZ Leiden, The Netherlands, http://www.leidencryogenics.com.

[7] A. Beyer, M. Kenyon, P. Echternach, B. H. Eom, J. Bueno, P. Day, J. Bock, et al. “Characterization of an Ultra-Sensitive Transition-Edge Sensor for Space-Borne Far-IR/Sub-mm Spectroscopy,” IEEE Transactions on Applied Superconductivity, vol. 21, no. 3, 2011, p.p. 199–202.

[8] M. D. Audley, G. de Lange, L. Ferrari,J.-R. Gao, R. A. Hijmering, P. Khosropanah, M. Lindeman, et al. “Performance of a Low-Noise Test Facility for the SAFARI TES Bolometer Arrays,” Journal of Low Temperature Physics, vol. 167, 2012, p.p. 208.

[9] D. Morozov, P. D. Mauskopf, P. A. R. Ade, M. Ridder, P. Khosropanah, M. Bruijn, J. van der Kuur, et al. “Ultrasensitive TES Bolometers for Space-Based FIR Astronomy,” IEEE Transactions on Applied Superconductivity, vol. 21, no. 3, 2011, p.p. 188–191.

[10] D. Drung., C. Aßmann, J. Beyer, A. Kirste, M. Peter., F. Ruede., and T. Schurig,). “Highly sensitive and easy-to-use SQUID sensors,” IEEE Transactions on Applied Superconductivity, vol. 17, no. 2, 2007, p.p. 699–704.

[11] Magnicon GbR, Lemsahler Landstraße,171, D-22397 Hamburg, Germany; http://www.magnicon.com.

[12] K.D. Irwin, G. C. Hilton, J. M. Martinis, and B. Cabrera., “A hot-electron microcalorimeter for X-ray detection using a superconducting transition edge sensor with electrothermal feedback,” Nuclear Instruments and Methods in Physics Research A, vol. 370, 1996, p.p. 177–179.

[13] P. F. Goldsmith, “Quasi-Optical Techniques,” Proceedings of the IEEE, vol. 80, no. 11, 1992, p.p. 1729–1747.